Eidgenössische Technische Hochschule Zürich
Swiss Federal Institute of Technology Zurich

Fabrication of a SNAIL Parametric Amplifier

Semester Thesis

Noah Kaufmann
knoah@ethz.ch

Laboratory for Solid State Physics
Departement of Physics, D-PHYS
ETH Zürich

Supervisor:
Marius Bild

July 23, 2021

Contents

Chapter 1

Introduction

1.1 Motivation

The simplest and most general definition of amplification is probably given by Clerk et al.. They state that "Amplification involves making some time-dependent signal larger" [1]. Before we turn to a more detailed picture of the amplification processes, we motivate amplifiers by explaining why "making some time-dependent signal larger" is crucial in circuit QED.

In the read-out of a superconducting circuit, the signal-to-noise ratio is critical. Among other things, the ratio influences how many repetitions of a measurement one has to do in order to get clear results or whether a single shot read-out is possible. The output from the read-out cavity can be considered a quantum signal since the transmission line's electromagnetic excitations involve only a few photons [2]. From this cold place to the measurement setup at room temperature, the initially already weak signal gets further attenuated, and thermic and electric noise adds to the signal. Already the noise floor of rf-lines at room temperature is far above the excitation of the initial signal. Therefore, it would be almost impossible to see any read-out signal without any kind of amplification of the original signal.

How now "making some time-dependent signal larger" helps maintain the initial SNR can be seen in Figure 1.1. While the amplifier itself adds some noise to the signal, the amplifier suppresses all losses and noises added to the signal after the amplifier by the amplification factor G. In practice, multiple stages of amplification are used. As shown in Figure 1.2, after the first amplification right at the cavity output, often high electron mobility transistors (HEMT) at 4 K and warm amplifiers at room temperature amplify the signal further.

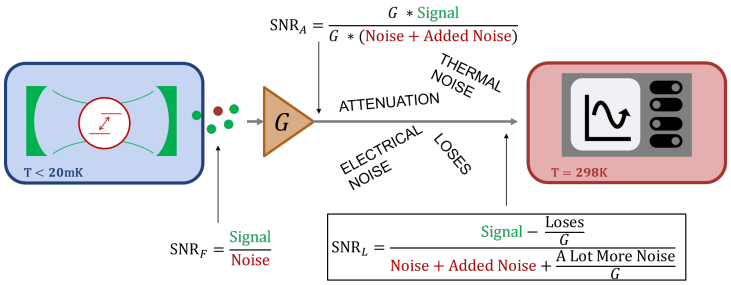

Figure 1.1: Cartoon of why amplification helps to suppress noise and losses.

1.2 Goals

In this project, we focused on the first amplification stage at the output of the read-out cavity. A simplified schematic picture of the used experimental setup is shown in Figure 1.2. Qubit, read-out cavity, and the first amplification stage are mounted on the ground plate of a dilution refrigerator below 20mK. The qubit read-out is done in the high-dispersive regime, and homodyne detection is used at room temperature to analyze the output of the fridge. The amplifier we use is called SNAIL Parametric Amplifier (SPA) and was developed in Yale [3] [4] [5]. Although we can make use of the fabrication recipe from Yale, so far we didn't manage to control some of the geometric characteristics of the SPA reliably. This made it challenging to influence some of the main properties of the SPA, for example, the frequency at which it is operating. This project aims to improve the geometric parameters in the fabrication process such that the process gets more reliable. In a next step an amplifier with suitable parameters for our point of operation should be fabricated. In the second part of the project, the goal is to assemble the SPA and integrate it into the measurement setup.

The first section in this thesis will touch on the theory of parametric amplifiers in general and the SPA in particular. In the main part of this text, the focus lies on the fabrication procedure of the SPA, and we conclude with a section about the characterization and tune-up of the SPA once it is inside the dilution refrigerator.

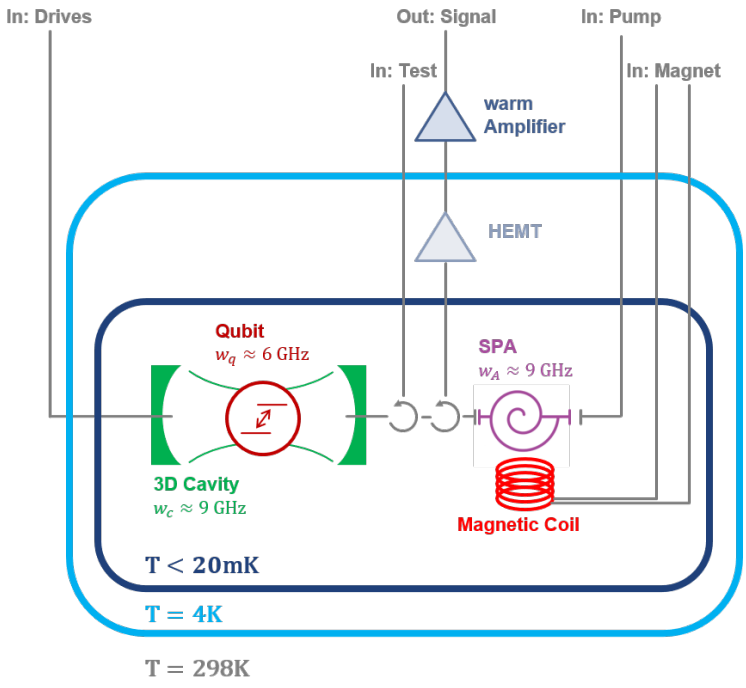

Figure 1.2: Simplified schematic of the fridge missing w&f and low-pass (ecosorb) filters after the cavity and at the 4K stage. Also any attenuation along the rf-lines is not included.

Chapter 2

Theory

In this chapter the different types of amplification are described. We will then turn to the SNAIL Parametric Amplifier and discuss the parameters that influence its specifications.

2.1 Parametric Amplifier

Parametric amplifiers can be categorized into several different types. A first differentiation can be made between phase preserving and phase-sensitive amplifiers. Furthermore, they can be divided into degenerate and non-degenerate, and into four-wave mixing and three-wave mixing. The type of an amplifier depends not only on the design of the parametric amplifier but also on the frequencies of the applied pump and the signal. In the following, the different types are briefly discussed.

2.1.1 Phase-Preserving and Phase-Sensitive Amplifier

We take a coherent state in the phase space to discuss the difference between phase-preserving and phase-sensitive amplification. Shown on the left side of Figure 2.1, the initial coherent state is in the phase space represented as a gaussian. The extent of the circle should represent the uncertainty in the two quadratures (I and Q) of the field. For the coherent state, the uncertainty in the two quadratures is symmetric and limited by the Heisenberg uncertainty. In Figure 2.1, the two possibilities to amplify such a state are presented. In the case that both quadratures are amplified equally, we talk of phase-preserving amplification [6]. The term phase-preserving refers to the fact that the phase of the amplified state is the same as the phase of the initial state. In contrast, only one quadrature is amplified in phase-sensitive amplification, while the other quadrature is deamplified. As a consequence, the phase-sensitive amplification of a coherent state leads to a squeezed state, as shown in Figure 2.1 [6]. Another fundamental difference between phase-preserving and phase-sensitive amplification is the minimum amount of noise they add to the signal. While a phase-sensitive amplifier can operate without adding additional noise, phase-preserving amplifiers will always add at least half-a-photon of noise [7].

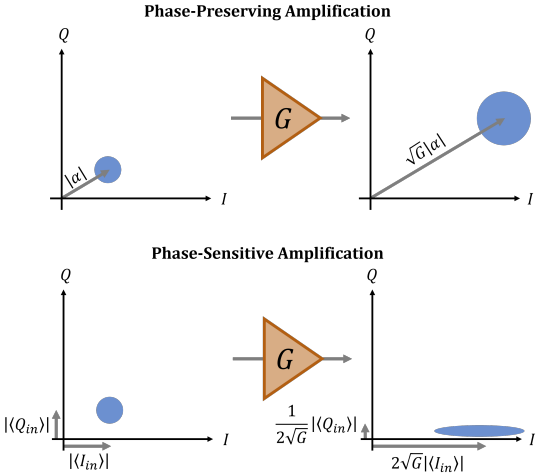

Figure 2.1: Phase-sensitive and phase-preserving amplification

2.1.2 Quantum Limited Amplifier

The goal of phase preserving parametric amplification is to amplify both quadratures of a signal by a gain G [8]. Here, we follow the Caves theorem in order to understand why this sort of amplification adds noise to the signal [9]. In a second quantization picture, the desired effect of the amplifier would be to multiply the creation and annihilation operator by the square root of the amplification gain.

$$\hat{a}_{out} = \sqrt{G} * \hat{a}_{in} \tag{2.1}$$

$$\hat{a}^{\dagger}_{out} = \sqrt{G} * \hat{a}^{\dagger}_{in} \tag{2.2}$$

This picture disregards that the operators have to fulfill the fundamental bosonic commutation relations $[\hat{a}, \hat{a}^{\dagger}] = 1$ [1]. With the definitions of (2.1) and (2.2) this is not the case since:

$$[\hat{a}_{out}, \hat{a}^{\dagger}_{out}] = G \neq 1 \tag{2.3}$$

To resolve this, one has to introduce an additional involved mode. This mode is called the idler mode [8].

$$\hat{a}_{out} = \sqrt{G} * \hat{a}_{in} + \sqrt{G-1} * \hat{b}^{\dagger} \tag{2.4}$$

$$\hat{a}^{\dagger}_{out} = \sqrt{G} * \hat{a}^{\dagger}_{in} + \sqrt{G-1} * \hat{b} \tag{2.5}$$

From (2.4) and (2.5), we can calculate the noise the amplifier introduces and reach:

$$n_{out} \geq G * n_{in} + (G-1) * n_{idler} \tag{2.6}$$

As the minimum value for n_{idler} is 1/2 a photon, in case the idler mode is in the

vacuum state to begin with, a phase preserving amplifier adds at least half a photon of noise [1]. Amplifiers that are close to this minimal introduced noise are called quantum limited amplifiers.

There are two intuitive pictures of why an amplifier should add noise to the signal. First of all, the no-cloning theorem states that the signal photons can not be perfectly replicated. Secondly, the noise is introduced by the amplification of the vacuum fluctuations of the idler mode [8].

In the case of phase-sensitive application, the commutation relation is preserved as only one quadrature gets amplified while the other quadrature gets deamplified (2.7) (2.8) and (2.9) [6]. Therefore, a phase-sensitive amplifier can operate without the addition of noise.

$$\hat{a}_{out} = \sqrt{G} * \hat{I}_{in} + i/(\sqrt{G}) * \hat{Q}_{in} \tag{2.7}$$

$$\hat{a}^{\dagger}_{out} = \sqrt{G} * \hat{I}_{in} - i/(\sqrt{G}) * \hat{Q}_{in} \tag{2.8}$$

$$[\hat{a}_{out}, \hat{a}_{out}] = 1 \tag{2.9}$$

2.1.3 Three-Wave and Four-Wave mixing

Very fundamentally, a parametric amplifier can be summarized as a device that converts, when stimulated by a signal field, energy from a pump field to a signal field and an additional idler field [8]. For this energy conversion, different nonlinearities can be used. We speak of three-wave mixing if a third-order nonlinearity is used. In that case, the pump is higher in frequency than the signal and the idler mode, and one pump photon is converted into a photon in the signal mode and a photon in the idler mode (2.10) [7].

$$\omega_{Pump} = \omega_{Idler} + \omega_{Signal} \tag{2.10}$$

In a four-wave mixing process, the fourth-order nonlinearity converts two pump photons into one signal photon and one idler photon (2.11) [7].

$$2 * \omega_{Pump} = \omega_{Idler} + \omega_{Signal} \tag{2.11}$$

2.1.4 Degenerate and Non-degenerate Amplifier

Depending on whether the idler mode is separated in frequency from the signal mode or not, an amplifier is considered non-degenerate or degenerate. For degenerate amplifiers, the pump source is at twice the frequency of the signal mode for three-wave mixing, respectively, at the frequency of the signal mode for four-wave mixing. For the three-wave mixing process this is shown in Figure 2.2. Amplifiers can also be spatially non-degenerate, meaning that idler and signal are at two spatially separated ports. Degenerate amplifiers are generally performing better in fast dispersive readout. Non-degenerate systems are preferable for multiplexed readout and measurement of correlation functions [10].

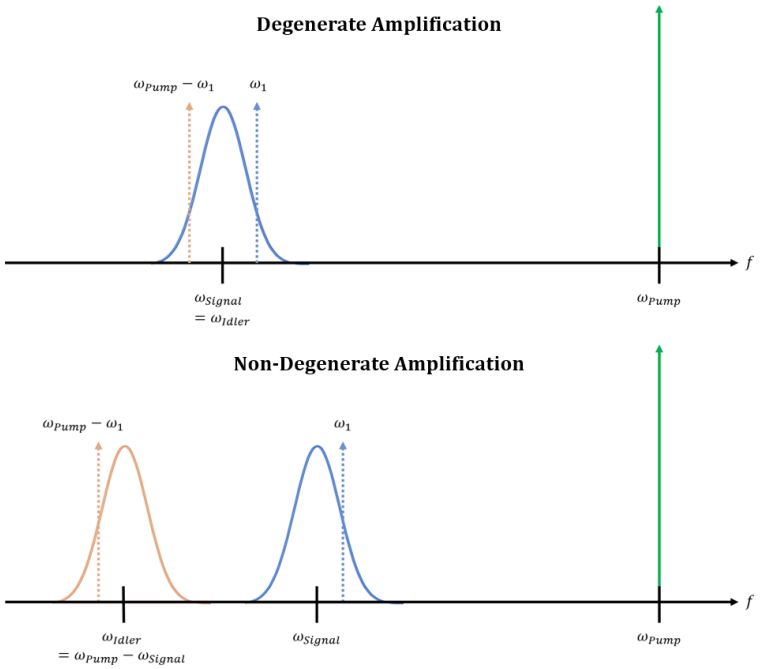

Figure 2.2: Frequency landscape for degenerate and non-degenerate amplification in a three-wave mixing process [7].

2.1.5 Operating Mode

All parametric amplifiers can be used in phase-preserving and in phase-sensitive mode [7]. The mode the amplifier operates in mainly depends on the applied frequency of the pump and therefore on whether it is operated degenerate or non-degenerate. For the case of a three-wave mixing amplifier, this depends on the frequency of the pump in the following way. If the pump is at exactly twice the frequency of the signal mode, it is not possible to distinguish signal and idler mode, because both modes are at the same frequency. Therefore, both parts, idler mode and signal mode, contain information about the initial signal [7]. This leads to phase-sensitive operation, and we operate the amplifier degenerate. If the pump is detuned from twice the signal frequency, we are operating in the phase-preserving mode [7]. In that case, the amplifier is non-degenerate.

2.2 SNAIL Parametric Amplifier (SPA)

We use a device called SNAIL parametric amplifier (SPA) at the first amplification stage at the output of the read-out cavity. The SPA is a near-quantum limited, three-wave mixing amplifier [3]. Currently we are operating the SPA as a non-degenerate, phase preserving amplifier. The SPA was developed in Yale [3] [4] [5]. We implemented the design of Yale without any fundamental changes and used some of their resources, namely gds-files and fabrication recipe, in the fabrication process of the amplifier.

2.2.1 SNAIL

The central element of the SPA is the Superconducting Nonlinear Asymmetric Inductive eLement (SNAIL). In order to perform three wave-mixing, one needs an asymmetrical potential around the minimum of the potential. This asymmetry is provided by the SNAIL. [4] The circuit diagram of the SNAIL is shown in Figure 2.3, it consists of one small Josephson in parallel to three large Josephson junctions. In the course of this project, we will tune two parameters of the SNAIL. The first parameter is the ratio between the inductance of the small Josephson junction to the inductance of the large Josephson junctions. This ratio is called α. And second, the inductance of the large Josephson junctions (L_J). The inductance can not only be changed by changing the size of the Josephson junctions but also by applying a magnetic flux to the Josephson junctions. The potential of the SNAIL is showed in Figure 2.3 and one can see the asymmetry in the potential around its minimum [4].

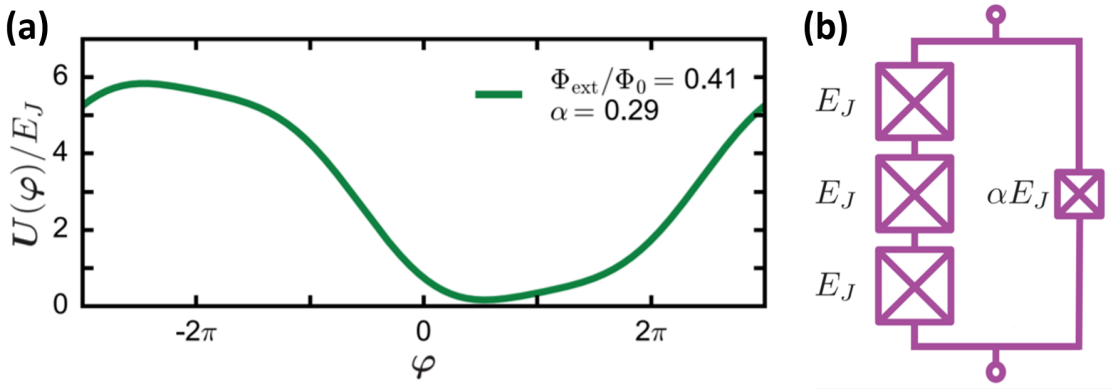

Figure 2.3: (a) Potential of a SNAIL [4]. (b) Circuit diagram of a SNAIL [4]. E_J is the Josephson energy which is related linearly to the Josephson inductance L_J. $E_J = I_C^2 * L_J$, with I_C the critical current of the junction [4].

2.2.2 Design

The SPA is created by placing 20 SNAILs at the center of a $\lambda/2$ section of a microstrip transmission line [3]. One end of the amplifier is coupled to the signal transmission line

and the other end to the pump. Figure 2.4 shows a schematic picture of the SPA and optical microscope images of a SPA from a SPA fabricated in Yale [5].

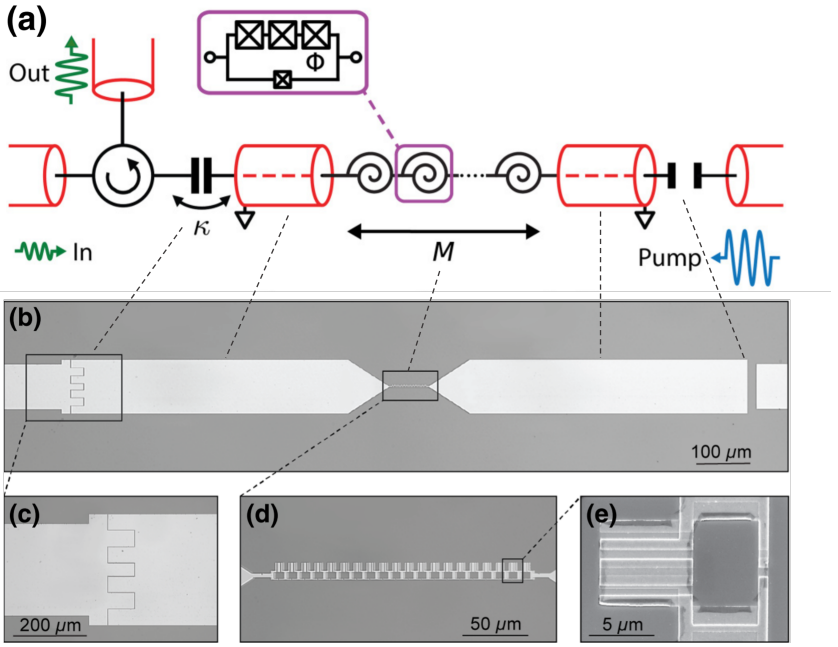

Figure 2.4: (a) schematic of a SPA (M corresponds to the number of SNAILs in the SNAIL array and κ is the coupling constant of the SPA to the signal port). Optical microscope images of (b) the microstrip resonator, (c) the capacitor that couples microstrip resonator to signal port, (d) the SNAIL array and (e) a single SNAIL [5]

2.2.3 Hamiltonian

The first few order terms of the Hamiltonian of the quantized system for the lowest frequency mode of the SPA can generally be written as [3]:

$$\frac{\hat{H}_{SPA}}{\hbar} = \omega_a \hat{a}^\dagger \hat{a} + g_3(\hat{a}^\dagger + \hat{a})^3 + g_4(\hat{a}^\dagger + \hat{a})^4 \tag{2.12}$$

In (2.12) g_3 corresponds to the 3rd order nonlinearity used for three-wave mixing amplification, g_4 is the Kerr nonlinearity. ω_a is the resonant frequency of the amplifier. Together with the coupling constant κ of the resonator to the signal port, the values of w_a, g_3, and g_4 determine the specifications of the SPA.

2.2.4 Specifications

One goal when designing a SPA is to minimize the Kerr nonlinearity. Because the Kerr nonlinearity limits over which range of signal powers, the amplifier amplifies with a

constant gain. For big g_4 terms, this so-called dynamic range is limited, because the Kerr non-linearity introduces frequency shifts at higher input powers and this then leads to an operating point of the SPA with lower gain [3]. Furthermore, it is crucial to have a nonzero g_3 term as this term is used for the three-wave mixing process. Nevertheless, g_3 should not be maximized as it also limits the dynamic range [3]. The resonance frequency of the SPA should be around the intended signal frequency to have sufficient gain. The coupling rate κ influences the bandwidth of the SPA as well as the maximum gain of the amplifier. As the bandwidth of the amplifier (B) gets bigger, the gain of the amplifier (G) gets more and more limited (2.13) [1]. Therefore one has to find a tradeoff. In the following, we will discuss how g_3, g_4, and ω_a are influenced by the geometric parameters of the SPA and how they affect the gain curve of the amplifier.

$$B \frac{\kappa}{\sqrt{G}} \tag{2.13}$$

Lumped-Element Model

In order to derive formulas for the frequency of the amplifier and to determine how the geometric design parameters affect g_3 and g_4, Frattini et al. took a lumped-element approach (Figure 2.5) [3]. The system is simplified to an array of M SNAILs with a linear inductance L_S, a capacitance C, and an inductance L. The linear inductance of the SNAIL can be expressed as $L_s(\phi_{ext}) = L_J/c_2(\phi_{ext})$. Where $c_2(\phi_{ext})$ is the second derivative of the potential of the SNAIL evaluated at its minimum and ϕ_{ext} is the applied magnetic flux.

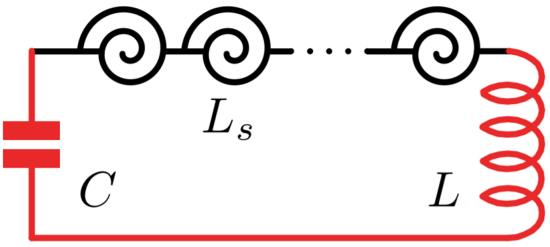

Figure 2.5: Lumped element model of SPA [3]

Frequency

From the circuit diagram in Figure 2.5, one can now calculate the resonance frequency of the SPA in the lumped-element model (2.14) [3].

$$\omega_a = \frac{1/\sqrt{LC}}{\sqrt{1 + M\frac{L_J}{L}/c_2(\phi_{ext})}} \tag{2.14}$$

From (2.14) we can analyze how the geometric design of the SPA and the applied magnetic flux influences the resonance frequency of the amplifier.

- The impedance of the microstrip resonator changes L and C.
- Number of snails (M) changes the total inductance of the SNAIL Array.
- The inductance of the large Josephson junction of the SNAIL (L_J) directly influences the linear inductance of the SNAIL (L_S).
- α changes the potential of the SNAIL and therefore influences c_2.
- The magnetic flux (ϕ_{ext}) changes the potential of the SNAIL and influences c_2.

While there are many different geometric parameters that influence the frequency of the SPA, all geometric parameters except α and L_J were left unchanged during the course of this project. As α was varied only in small ranges, we influenced ω_a by changing L_J. This was done by changing the area of the large Josephson junction and we will further discuss this in chapter 3. Once the SPA is mounted in the dilution refrigerator ϕ_{ext} is used to tune ω_a (chapter 4).

Third- and Fourth-Order Non-Linearity

Still following the lumped-element approach, expressions for g_3 and g_4 can be derived (2.15) (2.16) [3]. In this formulas c_2, c_3 and c_4 are the second, the third, respectively the fourth derivative of the potential of the SNAIL evaluated at its minimum. E_C is $e^2/2C$.

$$\hbar g_3 = \frac{1}{6}\left(\frac{\sqrt{M}L_s}{L+ML_s}\right)^2 \frac{c_3}{c_2}\sqrt{E_C \hbar \omega_a} \tag{2.15}$$

$$\hbar g_4 = \frac{1}{12} M \left(\frac{L_s}{L+ML_s}\right)^3 \left[c_4 - \frac{3c_3^2}{c_2}\left(1 - \frac{ML_s}{L+ML_s}\right)\right]\frac{E_C}{c_2} \tag{2.16}$$

As we see in (2.15) and (2.16), all in the section about the frequency listed geometric parameters also influence the non-linearity terms. In their analysis of the optimal geometric parameters, Fratini et al. show that the g_3 and g_4 term are especially sensitive to α [3]. α mainly influences the shape of the potential and therefore has direct influence on c_2, c_3 and c_4. Their theoretical and experimental analysis of different devices resulted in $\alpha = 0.09$ as a desirable value. In this project we aim for the same value.

Gain

From the Hamiltonian of the SPA and input-output theory, one can derive the phase preserving power gain [3].

$$G = 1 + \frac{4\kappa^2|g|^2}{((\Delta + (32/3)g_4|\alpha_p|^2)^2 - \omega^2 + \kappa^2/4 - 4|g|^2)^2 + (\kappa\omega)^2} \tag{2.17}$$

Where $g = 2g_3\alpha_p$, $\omega = \omega_s - \omega_p/2$ is the detuning of the signal from half the pump frequency, and $\Delta = \omega_a - \omega_p/2$ is the detuning of the SPA resonance frequency from half the pump frequency.

As visible in (2.17), the gain of the amplifier is influenced by the resonant frequency of the amplifier as well as by the nonlinearity terms and the coupling constant. Almost all geometric changes on the amplifier therefore change the gain curve. For achieving sufficient gain, it's especially important, that the detuning between ω_a and the signal frequency is small. Also the detuning of the pump from twice ω_a limits the gain.

Chapter 3

Fabrication

The central part of this project was to improve the SNAIL fabrication process such that one can reliably tune the α value and the junction size. The goal was to create a SPA with a resonance frequency at about 9 GHz and an α value of 0.09. The target for the α value comes from the derivation by Frattini et al. [3], and the target frequency corresponds to the resonant frequency of the used read-out cavity. In this section, the fabrication process is described, and the problems that occurred during the fabrication iterations are discussed.

3.1 Shadow Evaporation Technique

The Josephson junctions are created using the shadow evaporation technique [11]. The fabrication procedure, displayed in Figure 3.1 with the example of the three Josephson junctions, starts by spinning two layers of resist on the wafer (step 1 in Figure 3.1). Parts of the resist are then exposed in ebeam lithography (step 2 in Figure 3.1). After developing, the mask for evaporation consists of 2 Dolan bridges for the triple junction and one Dolan bridge for the single junction (step 2 in Figure 3.1). The gds file used to create the mask and slices through the mask are shown in Figure 3.2. Afterwards, aluminum is evaporated at a certain angle onto the wafer (step 3 in Figure 3.1). Each Dolan bridge throws a shadow on the wafer where no aluminum is deposed. Then the aluminum is oxidized in order to create a layer of resistance on the aluminum (step 4 in Figure 3.1). The process is continued by evaporating aluminium with the opposite angle onto the wafer (step 5 in Figure 3.1). The shadows from the Dolan bridges are now at different places than the shadows of the first evaporation and Josephson junctions are created between two shadows. During the liftoff we get rid of the resist layer and the unnecessary aluminum sticking on the resist. In step 6 of Figure 3.1 one sees the created tripple junction.

The most important geometric parameters of the mask and the sizes of the junctions are shown in Figure 3.3, the corresponding values of the used masked are noted in Table 3.1.

3.2 DC Probing

During the DC probing one measures the room temperature resistance across a SNAIL array. Here, the aluminum is not superconducting, and for DC probing the SNAIL can be modelled with the circuit diagram shown in Figure 3.4.

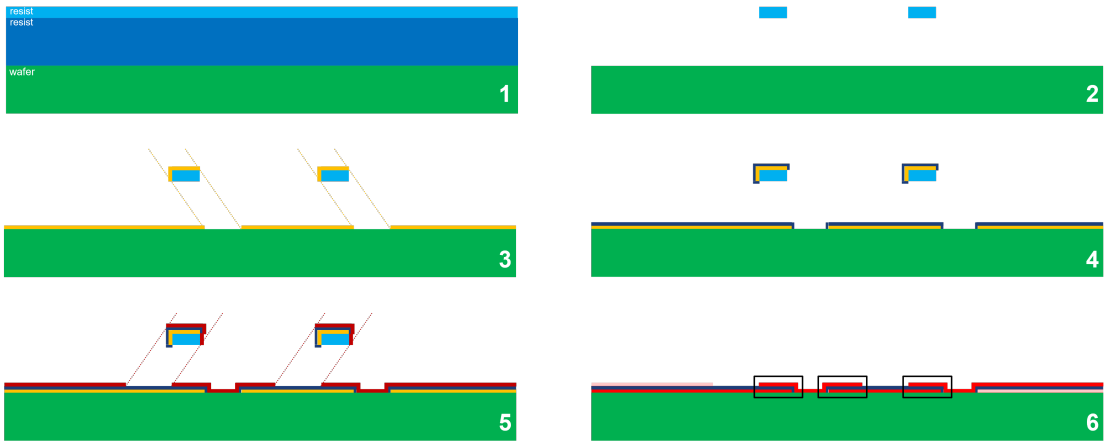

Figure 3.1: 1. wafer (green) with two layers of resist on top (two shades of blue), 2. Mask after developement of the resist, 3. first aluminum evaporation, 4. oxidation of aluminum, 5. second aluminum evaporation, 6. final triple Josephson junction (marked by black rectangle)

parameter	value
w_{bridge}	$0.5\mu m$
w_{btwn}	$2.2\mu m$
h_1	$0.85\mu m$
h_2	$1.05\mu m$

Table 3.1: table of the most important mask parameters

In the fabrication iterations different combinations of α values and junction areas were tested. To do this compactly, we did not always integrate the SNAIL array into a microstrip resonator transmission line (Figure 3.5), but instead just fabricated the SNAIL array. Such a test structure is shown in Figure 3.6, and we applied the same concept to test different e-beam doses for exposing the areas on and around the Dolan briges.

Information about the size of the large Josephson junction and the size of the small Josephson junction are gathered by creating SNAIL arrays that consist only of large, respectively, only of small Josephson junctions. Those arrays are created by leaving the whole array unchanged except that all small or all large junctions are left open, meaning that a gap with no aluminum replaces the Josephson junctions. A picture of open small junctions is shown in Figure 3.7.

In addition to the SNAIL arrays with open short and open long junctions, there is also a test structure fabricated where all junctions are shorted. This measurement is used to account for other sources of resistance in the calculation.

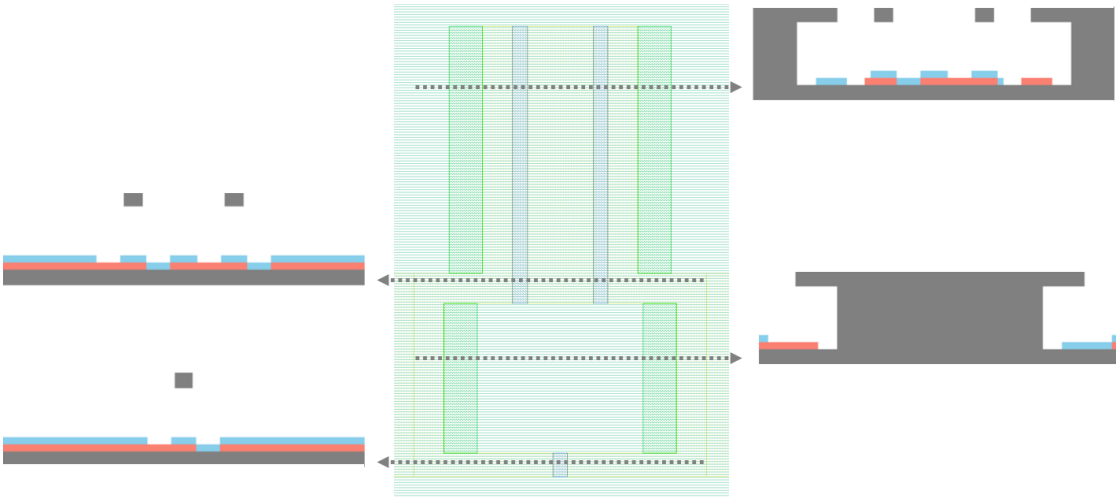

Figure 3.2: Screenshot of the gds file used to create the mask for the evaporation of the SNAIL. On the side slices through the mask are shown. The orange and blue colour represent the evaporated aluminum

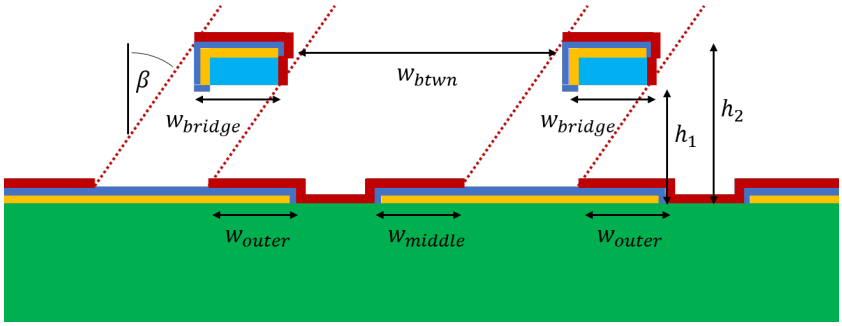

Figure 3.3: Geometric parameters of mask, evaporation angle and junction sizes for the triple junction.

3.2.1 Alpha

Alpha (α) is defined as the ratio of the inductance of the small Josephson junction to the inductance of the large Josephson junction. As the inductance of the Josephson junction is proportional to the area, α can be expressed in terms of the junction areas as:

$$\alpha = \frac{A_{smalljunction}}{A_{largejunction}} \tag{3.1}$$

At room temperature the resistance of the Josephson junctions is connected to the area of the junction by the resistivity of the aluminum-oxide (ρ) and the thickness of the

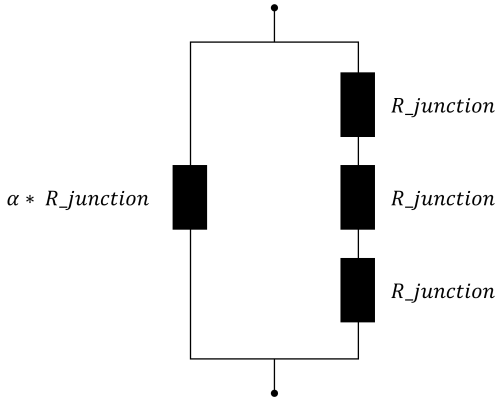

Figure 3.4: Circuit diagram of a SNAIL at room temperature

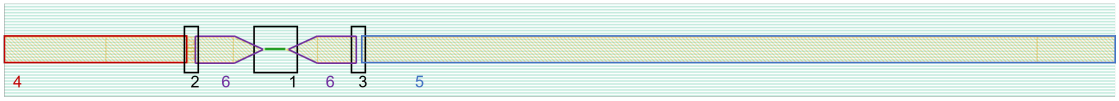

Figure 3.5: Screenshot of gds-file of the complete SPA with different components framed in different colors. 1. SNAIL array, 2. coupling to signal line, 3. coupling to pump line, 4. signal port, 5. pump port, 6. microstrip transmission line

aluminium-oxide (t):

$$R_{junction} = \frac{\rho * t}{A_{junction}} \tag{3.2}$$

Combining (3.1) and (3.2), one can express the α value in terms of the measured resistances:

$$\alpha = \frac{R_{largejunction}}{R_{smalljunction}} \tag{3.3}$$

3.2.2 Frequency

As stated in (2.14), the frequency of the SPA is determined by many different parameters. Therefore, the relation between resistance and frequency is not as simple as it was for the α value of the SNAIL. In (2.14) L_J depends on the area of the large junction (A_J). This relation is linear and depends on the critical current density of aluminum (J_c) and the superconducting magnetic flux quantum (ϕ_0):

$$L_J = \frac{\phi_0 J_c}{2\pi} A_J \tag{3.4}$$

The resistance of the SNAIL array is connected to the area of the large junctions by the resistivity of the aluminum-oxide (ρ), the thickness of the aluminiumoxide (t), the number of SNAILs per array (M) and α:

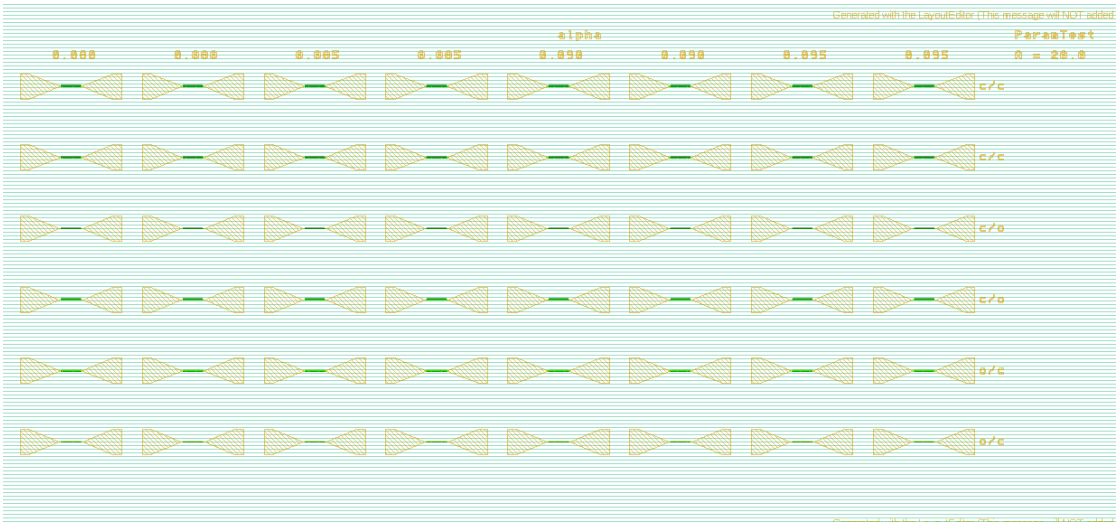

Figure 3.6: Screenshot of gds-file of a teststructure. Sweeping α over the columns and with different junctions left open across the rows.

$$A_J = \frac{M\rho t}{R_{array}} \frac{1}{\alpha + \frac{1}{3}} \tag{3.5}$$

Using (3.4) and (3.5), we can find, up to a constant factor, the relation between the resistance of the SNAIL array (R_{array}) at room temerpature and the inductance. This constant is dependent on the critical current density of superconducting aluminum, the resistivity of aluminum oxide as well as the thickness of the resistance layer.

3.3 Scanning Electron Microscope (SEM) Analysis

Under the scanning electron microscope, one can clearly see the Josephson junctions (for example Figure 3.8). Especially to find out the right doses for the e-beam, this is very helpful. The SEM pictures are very useful to judge the quality of the SPA. Out of the measured junction sizes one can also calculate the corresponding α. Still, because there is the chance that the interaction with the electrons during the microscopy damages the SPA, we avoid making SEM pictures of the chip that will be further processed to an amplifier.

3.4 Geometrical Improvements

In order to be able to control the α value of the SNAILs reliably and to find an overall resistance that corresponds to the correct resonant frequency of the SPA, especially two problems were important to solve. Initially, as shown in Figure 3.8, the triple junction of the SNAIL varied largely in size, and the outer junctions were shaped like the letter L.

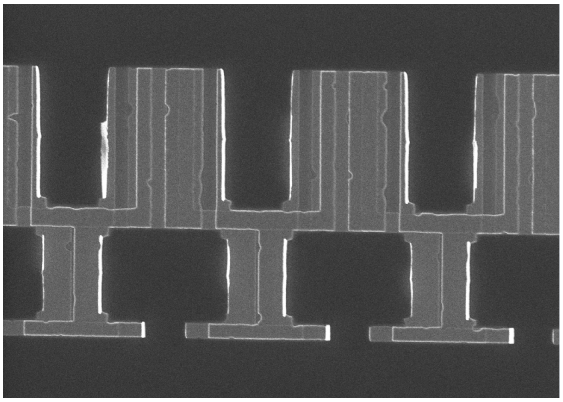

Figure 3.7: SEM picture of a SNAIL with the small junction left open in order to measure the resistance of the large junctions.

As a useful tool to elaborate the fabrication process, I developed a drawing routine that simulates the fabrication process. In the routine, the geometry of the mask, the heights of the resist, and the evaporation angle can be changed. A simple 2D ray tracing of the evaporated aluminum is then used to simulate SEM pictures and calculate the junction sizes. Besides the SEM simulation, the routine also creates pictures of slices through the mask. A picture of the drawing routine is shown in Figure 3.9.

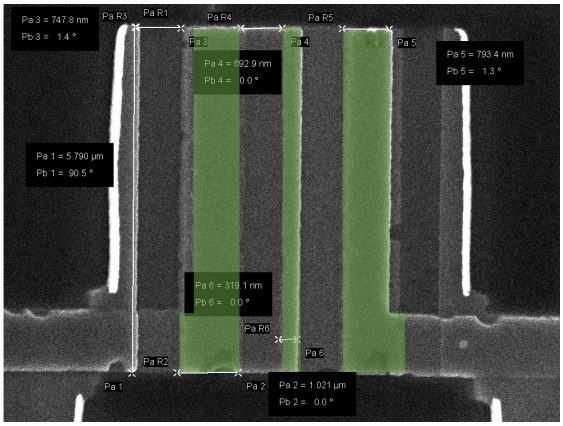

Figure 3.8: SEM picture of SNAIL displaying the L-shaped junctions as well as the difference in size of the junctions.

3.4.1 Equally Big Triple Junctions

The SPAs produced previous to this project had the problem that the junctions were not equal in size. The formula for the size of the junctions as a function of the evaporation angle and the mask geometry is given in (3.6) and (3.7).

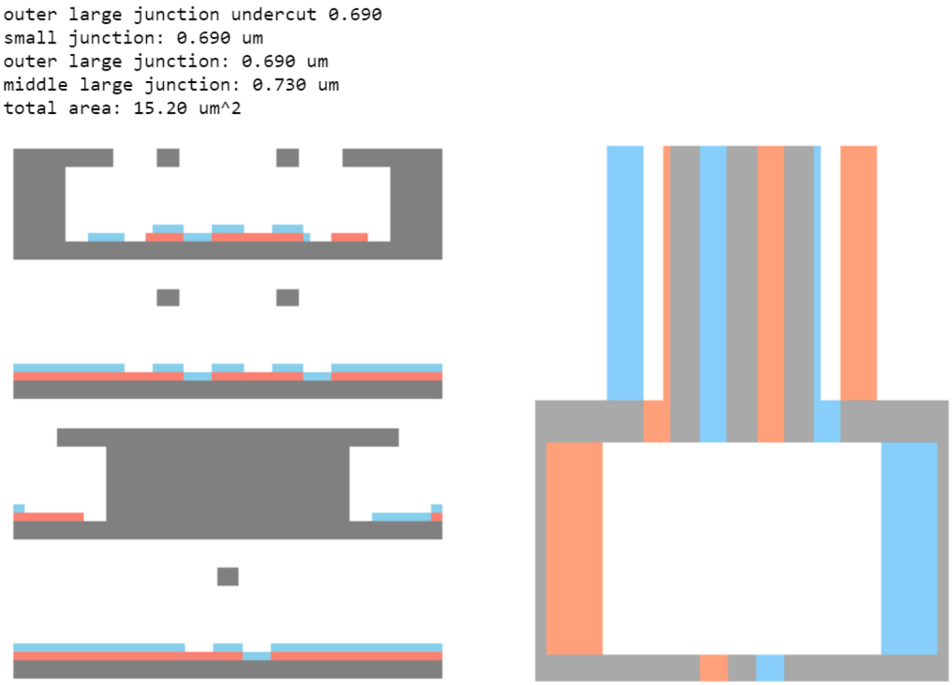

Figure 3.9: Output pictures of the drawing routine. In the right picture, the orange color represents places where there is only aluminum that was evaporated from the left side, the blue color represents places where there is only aluminum that was evaporated from the right side and the grey color represents places where both aluminum layers overlap and junctions are built. On the left side vertical slices at different positions are shown. On top the sizes of the Josephson junctions are outputted.

$$w_{outerjunction} = 2 * h_1 * \tan\beta - w_{bridge} \tag{3.6}$$

$$w_{middlejunction} = w_{btwn} - 2 * h_2 * \tan\beta \tag{3.7}$$

The main challenge in order to make all junctions equal in size was that we had no exact knowledge about the exact thickness of the resistors, since we had no spinning curve for this particular resist on the used wafer. While we always used the same mask geometry for all fabrication iterations, we varied the angle. By measuring the junction sizes in the SEM images (Figure 3.8), we then calculated the resist layer thickness by (3.8) and (3.9), where β is the evaporation angle used for sample production of the SEM image shown in Figure 3.8. Having an estimate for the height of the resist layers we calculated the angle for equally sized junctions (β_{opt}) according to (3.10).

$$h_1 = \frac{w_{outerjunction} + w_{bridge}}{2 * \tan\beta} \tag{3.8}$$

$$h_2 = \frac{w_{btwn} - w_{juntionmiddle}}{2 * \tan\beta} \tag{3.9}$$

$$\beta_{opt} = \arctan\left(\frac{w_{bridge} + w_{btwn}}{2 * (h_1 + h_2)}\right) \tag{3.10}$$

3.4.2 L-Shaped Junctions

As visible in the top right picture of Figure 3.2 the top resist layer is further expanded than the lower resist layer. This structure is called undercut. It prevents the evaporated aluminium to stick at the connection of wafer to bottom resist layer. Such a connection would disturb the liftoff and possibly damage the aluminum layer. The phenomenon of the outer junctions being L-shaped occurs (Figure 3.8 and Figure 3.12), because for large enough angles, the undercut also throws a shadow that becomes relevant for the junction size. To avoid this, one can increase the gap in the mask between the undercut and the Dolan bridge. As our final evaporation angle was small enough, the problem was solved without any change on the mask geometry.

3.5 Fabrication Iterations

During this project, a total of four fabrication iterations were made. In this section, the findings and problems of each fabrication run are described.

3.5.1 w2109B

In addition to one dose test and seven normal SPAs, the chip included four test structures. Each test structure included seven different α values, and each test structure had a different junction size. Several problems occurred in this first iteration.

The values measured in the DC-Probing were very inconsistent. Equivalently designed structures varied a lot in the measured resistance. Consequently, as one sees in Figure 3.10, the designed α values did not correlate with the measured α values. In order to find the reason for this, we decided on making SEM pictures of the junctions, and two problems were found (Figure 3.11). Firstly the large junctions were not equal in size, and the outer junctions had an L-shape. Secondly, and probably more important for the inconsistent resistance measurements, the small junctions were partially shorted, and the junctions were rounded off. In order to correct for the unequal junction sizes, we decided on changing the evaporation angle for the next iteration. To find the reason for the bad quality of the small junctions, we decided on testing different doses.

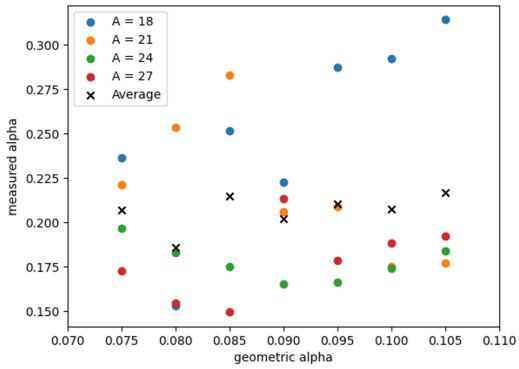

Figure 3.10: Designed α values plotted against measured α values of the 1st fabrication iteration.

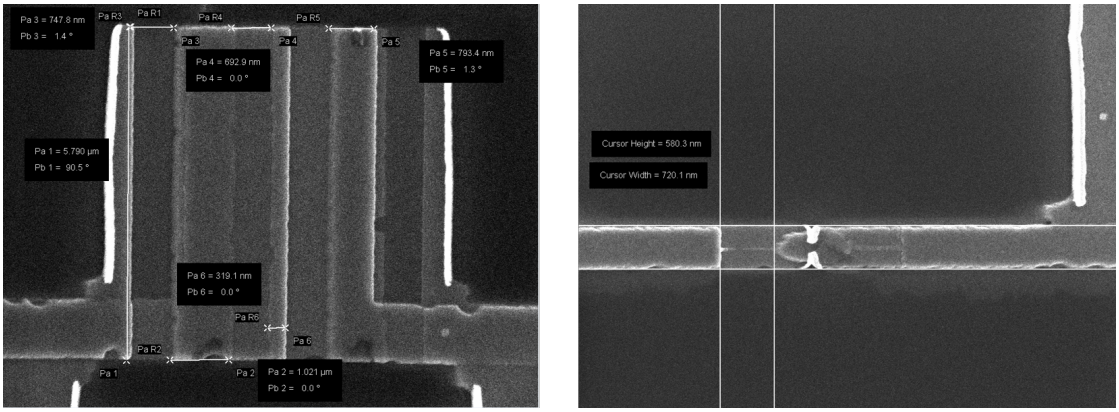

Figure 3.11: SEM picture of the large and the small junctions. While the thin line next to the small junction indicates that the junction is shorted.

3.5.2 w2124A

In the second iteration of the project, we tested a broad range of different doses. Additionally to the dose tests, there were several test structures for different α values and areas on the chip.

The SEM pictures showed that the problems that occurred with the small junction in the previous iteration did not show up at any dose. Further investigating into that, we found that the used resist layer in the first iteration was about a year old and might have suffered in quality during that time. We decided not to change the doses for the next iterations. On the other hand, the inequality in the size of the junctions even got bigger, and also the L-shape of the outer problem was stronger visible (Figure 3.12). Both of these findings lead to the suspicion that the evaporation device uses the opposite angle than we did in our calculations. This suspicion turned out to be true, and with (3.8)

and (3.9) we calculated the expected resist layer heights again and from there the new evaporation angle (3.10).

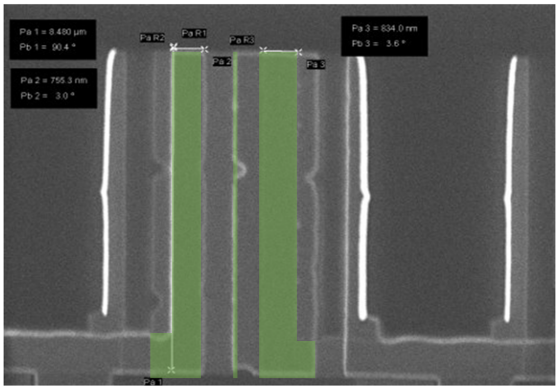

Figure 3.12: SEM picture of the 2nd iteration in fabrication. The junctions are highlighted in green. The middle junction is almost disappearing and the outer junctions are L-shaped.

3.5.3 w2124B

In the third iteration, we again tested for different α values at three different junction areas.

The junctions were almost equal in size, and the L-shape disappeared (Figure 3.13). The data of the DC test is shown in tabular 3.2. For the larger junction sizes (area $20\mu m^2$ and $18\mu m^2$), the difference between designed and measured α was a lot smaller than initially. For the smaller junctions with size with a combined area of $16\mu m^2$, the difference between designed and measured α is still significant. As the $16\mu m^2$ junctions' overall resistance indicated a wrong frequency, we decided not to investigate that problem. Instead, we focus on improving the equality of the junction sizes by further tuning the evaporation angle.

area $[\mu m^2]$	designed α	measured α
16	0.09	0.196
18	0.09	0.106
20	0.09	0.093

Table 3.2: results 3rd iteration

3.5.4 w2124C

Optimistic that we were ready to create valuable chips in the 4th iteration, we made a chip with 9 SPAs, two test structures for DC probing whether we were able to fabricate the designed α values, and one dose test.

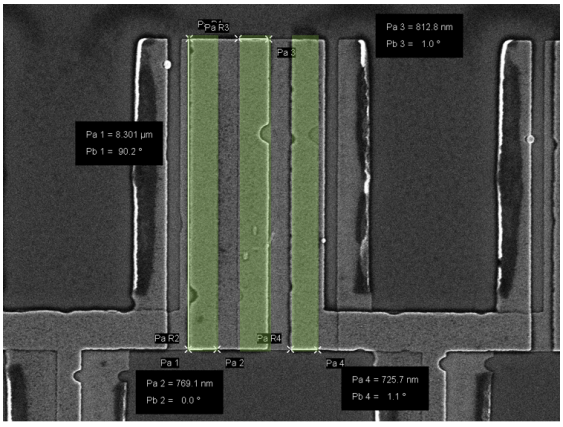

Figure 3.13: SEM picture of the 3rd iteration in fabrication. The junctions are highlighted in green.

The measured α values corresponded very well with the designed α value, as shown in Figure 3.14. Therefore, the chip was not put under the SEM in order to not destroy any of the structures. The 9 SPAs included 3 SPAs with a promising total resistance. We decided to use two of them for the further processing of the parametric amplifier.

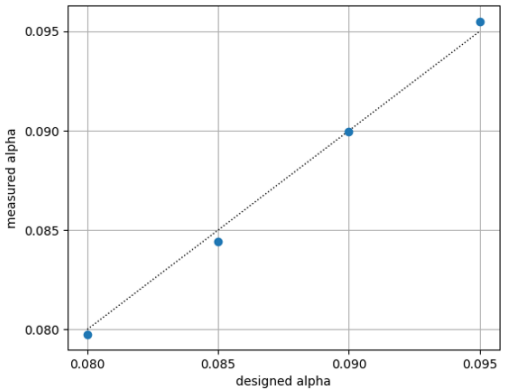

Figure 3.14: Designed α values plotted against measured α values of the 4th fabrication iteration.

3.6 Assembly

The assembly involves packaging the SPA chip into a copper dual-port device with an integrated magnetic coil. The main steps in integrating the chip are the following:

1. Evaporate a silver ground plate on the backside of the chip.

2. Dice the chip. One has to be careful in order to not damage the silver ground plate.
3. The copper box is cleaned with alconox, acetone and methanol.
4. A circuit board, where the SPA chip is later put on, is cleaned with sand paper and isopropanol (IPA) and than put into the copper box.
5. By using a hotplate, the circuit board is soldered to the copper box.
6. Pins are put through the copper box and soldered to the circuit board.
7. The SPA chip is wirebonded onto the circuit board.
8. The magnetic coil is integrated into the copper box.

The assembled SPA without the magnetic field coil and before the lid is put on is shown in Figure 3.15.

Figure 3.15: Assembled SPA without the lid and the magnetic field coil.

Chapter 4

Integration into Measurement Setup

The first step of the integration of the SPA consists of mounting the SPA on the ground plate of the dilution refrigerator and connect the rf-lines as shown in Figure 1.2. After this is done and the fridge is cooled down below 20mK, two more important steps have to be done before one can start measuring qubits. First, the relation between applied magnetic flux and resonant frequency of the SPA has to be found. In a second step, this relation is used to tune the pump frequency and the magnetic flux, such that the intended operating point is reached. Once the SPA is ready for measurement, one can also measure other important characterizations such as the 1dB compression point or the noise visibility ratio (NVR). The SPA that resulted from the fabrication described in chapter 3, was only finished by the end of this project. Therefore, all in this chapter described steps were conducted on a SPA from a previous fabrication iteration. As we will see in Figure 4.2 the resonance frequency of this SPA was to low and the cavity had to be adjusted in order to be able to make use of the SPA.

4.1 Characterisation

The relation between the applied magnetic flux and the resonant frequency of the SPA is characterized by observing the phase shift of a signal reflected by the SPA for different signal frequencies. This measurement is done by connecting the vector network analyzer (VNA) with the In: Test port and the Out: Signal port of the fridge (Figure 1.2). The VNA then measures the phase shift between the signal inputted into the fridge and the signal outputted. When the input frequency is not in resonance with the cavity, the signal just gets reflected at the SPA and picks up a phase of 180 degrees. If the input frequency hits the resonant frequency of the SPA, the outputted signal picks up no phase. In case the frequency is not at the resonant frequency but within the bandwidth of the SPA, the signal picks up some positive or negative phase dependent on whether it is positively or negatively detuned. We can, therefore, observe a phase change from + 180 degrees to – 180 degrees centered at the resonant frequency of the SPA by sweeping over the frequency. One such sweep is shown in Figure 4.1.

Following the inputted signal in Figure 1.2 one sees, that the signal also gets reflected by the cavity. The phase shift from the reflection at the cavity does not disturb our measurement since the linewidth of the read-out cavity is much smaller than the SPA bandwidth. Furthermore, one also has to calibrate the VNA to the phase shift added to its signal by traveling through the cable.

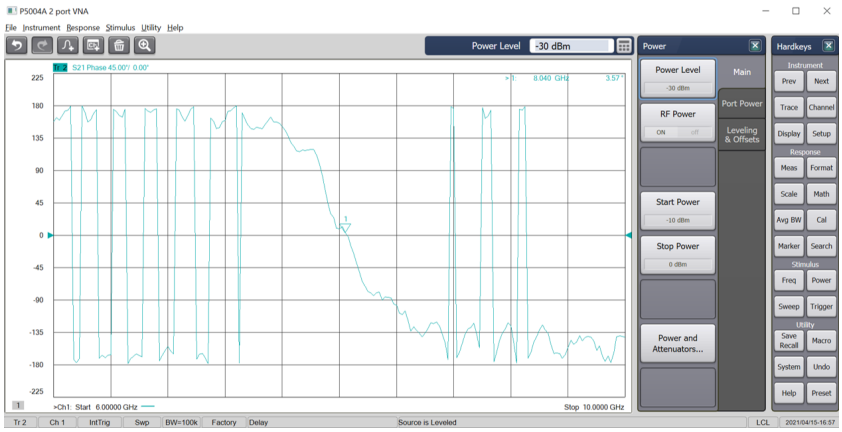

Figure 4.1: Screenshot of a VNA sweep. The resonant frequency of the SPA is at the point where there is no phase shift.

To see how the magnetic flux shifts the resonant frequency, a 2D sweep over frequency and magnetic flux is performed. For each frequency sweep of the VNA, a different magnetic current is applied to the magnetic coils. This measurement leads to Figure 4.2. When analyzing Figure 4.2, it is important to keep in mind that -180 degrees and 180 degrees are essentially the same, and therefore the sharp line at approximately 10.5 GHz does not indicate any fast phase shift. The interesting things happen between 7GHz and 9GHz. Here we see that the phase shift crosses 0, thus indicating the resonance frequency of the SPA for a particular magnetic flux. It is also well visible how the relation between magnetic flux and the resonant frequency is periodic. One period corresponds to one flux quantum through the loop of the SNAIL. As figure Figure 4.2 shows, the resonant frequency of the SPA is tunable between approximately 7.2GHz and 9GHz by applying a magnetic flux.

4.2 Tune-up

In a world with perfect 3-wave-mixing, degenerate amplifiers, all steps after the characterization would be straightforward. In reality, we have to deal in particular with two phenomena when turning on the pump. The first issue is the non-zero Kerr nonlinearity. This term shifts the resonance frequency of the SPA when higher power is applied to the resonator. The second issue is that the SPA also spontaneously down converts pump photons to two photons at half the frequency of the pump. We decide to detune the peak of the gain curve by 1MHz to the cavity frequency such that the spontaneous down-conversion does not disturb the read-out signal. In order to tune up the pump, we follow the following procedure:

1. Connect the VNA with the In: Test port and the Out: Signal port (Figure 1.2) and observe the transmission spectrum.

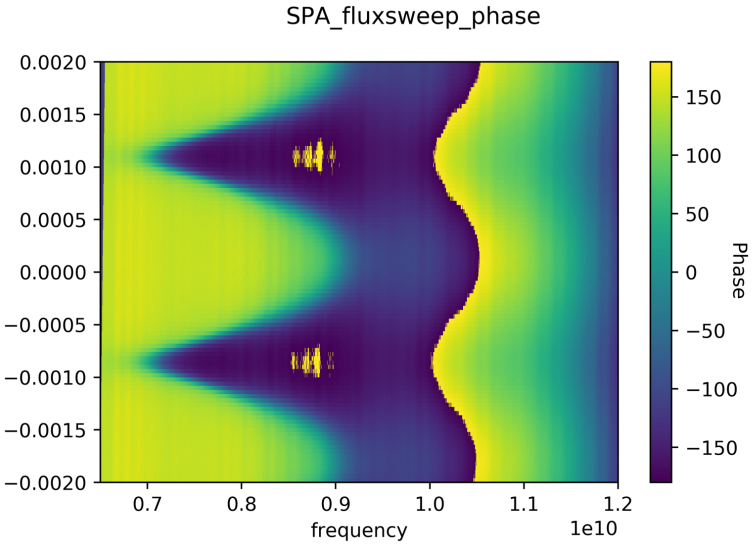

Figure 4.2: Plot of the phase shift of a signal reflected by the SPA, as a function of the applied current to the magnetic coils on the y-axis and the signal frequency on the x-axis.

2. Use the relation from Figure 4.2 to find the magnetic flux at which the resonance frequency of the SPA is at the frequency of the read-out cavity. The SPA is designed such that the steepest part of the asymmetric potential is around the cavity frequency. We can see from figure Figure 4.2 that therefore the ideal cavity frequency would be around 8GHz.

3. Turn on the pump and change its frequency until a gain curve can be seen in the transmission spectrum. Tune the pump frequency further until the gain is maximal. The pump frequency should be at twice the resonance frequency of the SPA. The peak of the gain curve is at half the pump frequency.

4. Tune the pump power such that the maximal gain is about 20dB.

5. To prevent spontaneous down-conversion from interfering with the cavity read-out signal, one has to detune the peak of the gain curve by about 1MHz from the cavity frequency. This detuning is done by shifting the pump frequency. If this process decreases the maximum gain of the SPA significantly, one has to tune the magnetic flux again to shift the resonance frequency on half the frequency of the pump.

Figure 4.3 illustrates the frequency of down-converted pump photons, the spectrum from the read-out cavity, and the gain curve with their corresponding bandwidth. One sees that by detuning the maximum peak of the gain curve by 1 MHz to the cavity, the down-converted photons do not interfere with the read-out signal from the cavity. Furthermore, the detuning has little influence on the gain of the signal photons as the

bandwidth of the gain curve is much bigger than 1MHz. The measurement of this situation for different read-out powers is shown in Figure 4.4.

As described in subsection 2.1.5, the detuning of the signal frequency with respect to half the pump frequency leads to a non-degenerate operation point. Therefore, we have a phase preserving amplifier. In order to have a degenerate phase-sensitive amplifier, we would have to use the pump at twice the signal frequency and ideally tune the SPA resonance frequency to the signal frequency to have maximal gain. In that case, it would be challenging to deal with the spontaneously down-converted pump photons.

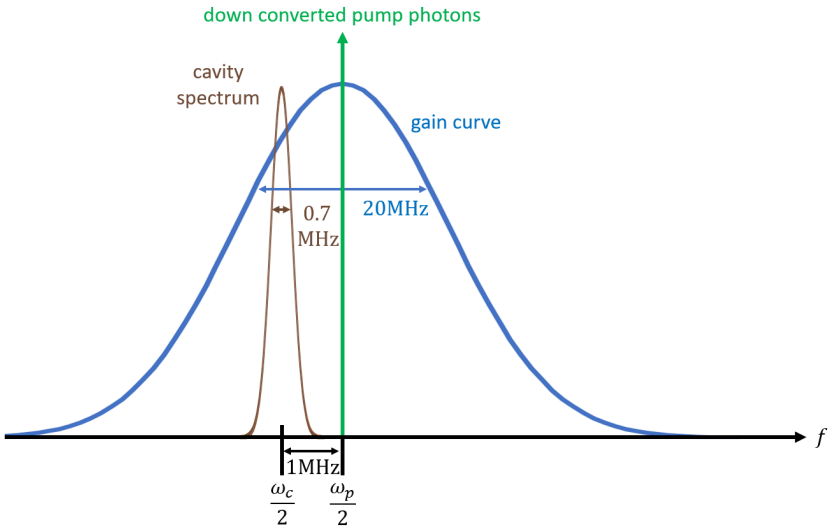

Figure 4.3: Out of scale frequency landscape and gain curve around resonant maximum of gain curve. w_p is the pump frequency and w_c the cavity frequency

4.3 Noise Visibilty Ratio (NVR)

The NVR is the ratio of the measured noise when the SPA is on (N_{on}) to the measured noise when the SPA is off (N_{off}) (4.1). In order to do this measurement the signal input P_{in} is set to zero. For the treatment everything in the transmission line after the SPA is lumped together and called System (Figure 4.5).

$$NVR = \frac{N_{on}}{N_{off}} = \frac{G_{Sys}G_{Spa}(N_{add} + \frac{1}{2}) + G_{Sys}N_{Sys}}{G_{Sys}N_{Sys}} = \frac{G_{Spa}(N_{add} + \frac{1}{2}) + N_{Sys}}{N_{Sys}} \tag{4.1}$$

As one can see in (4.1) NVR gets smaller the less noise the SPA introduces. Therefore in the design of the SPA a small NVR is generally desirable. But one has to be careful, a small NVR is not necessary a sign of little introduced noise from the SPA, but could also come from a lot of noise in the system.

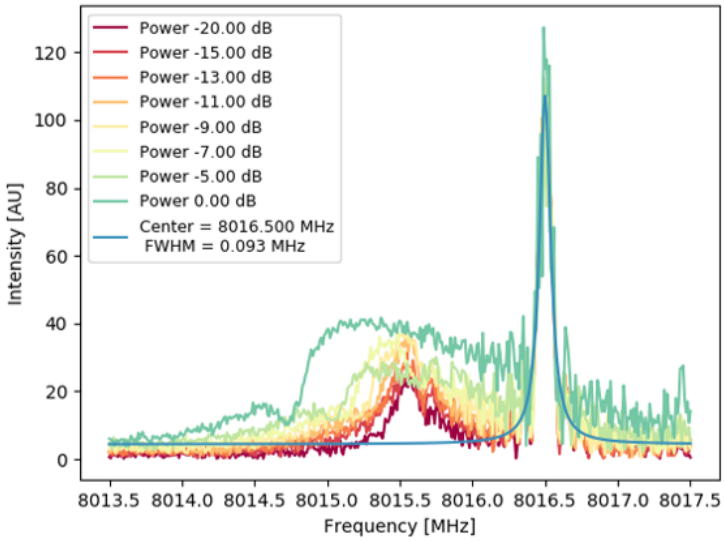

Figure 4.4: Cavity spectroscopy for different read-out power. The peak at 8015.5MHz corresponds to the cavity spectrum and the peak at 8016.5MHz is generated by down-converted pump photons.

4.4 1dB Compression Point

For low powers the gain is independent of the signal power. If we start to increase the signal power at some point the gain starts to decrease. This gain compression has two causes. First, the Kerr nonlinearity leads to a shift of the SPA resonant frequency. As the signal power gets higher this shift lowers the gain of our signal [3]. Secondly, pump depletion leads to further gain compression [3]. The 1dB compression point characterizes at which signal power the gain is 1dB lower compared to low signal powers. This is measured by steadily increasing the power of the VNA until the observed gain droppes by 1dB. The measurement is shown in Figure 4.6.

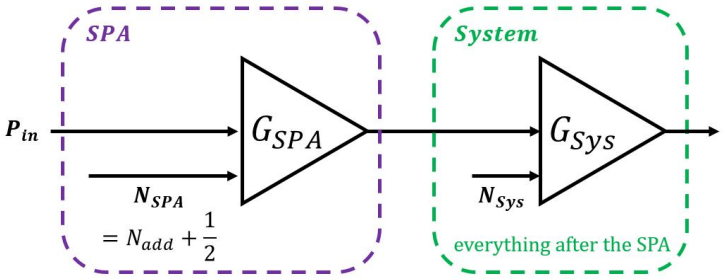

Figure 4.5: The setup is split into two parts (SPA and System). Both parts introduce noise (N_{SPA} and N_{Sys}). P_{in} is the signal input and G the gain of the two parts.

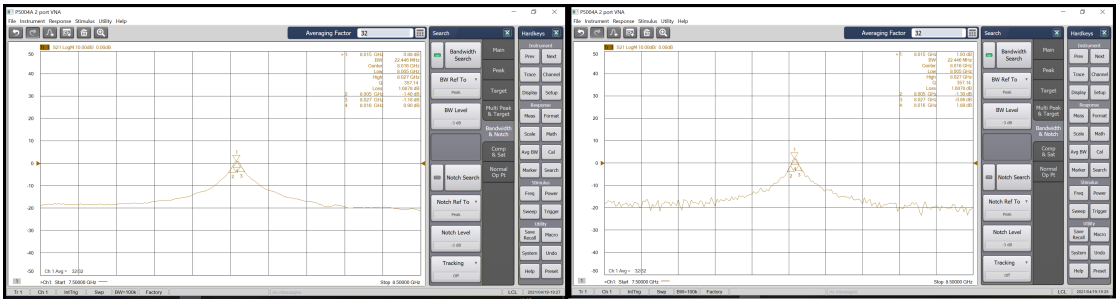

Figure 4.6: At input power of $-60dBm$ the gain of the SPA saturated. The power is increased until at $-38dBm$ the gain is $1dB$ lower than at $-60dBm$. As the input line contains approximately $60dB$ of attenuation the measured $1dB$ compression point is at approximately $-100dBm$

Chapter 5

Conclusion

The goal of this thesis was to fabricate a SPA with the desired frequency and an α value of 0.09. Moreover, the SPA should be tuned up and characterized. The fabrication part of the thesis took more time than expected as we realized that there is a fundamental error in our fabrication procedure. In several iteration steps, we were able to identify the evaporation angle as the source for the difference between the designed geometry and the fabricated SPA. In this process, I developed a drawing routine that is generally helpful to simulate the shadow evaporation technique. By adjusting the angle, we reliably reproduced in fabrication the designed SPA and created SPAs with the desired α values. In the future, with the fixed evaporation angle, the drawing tool to calculate the resist thicknesses, and the reorganized code to create the gds file, it will be easier to iterate the SPA and change geometric parameters.

As the SPA with the correct α value was only finished at the end of the semester, I could not characterize and tune up the designed SPA. Therefore, the integration of the SPA into the dilution refrigerator will be the next step. It will be interesting to see whether it will perform better than the currently used amplifier. To still get a picture of the whole process, I took part in the characterization and the tune-up of an old SPA and helped with the postprocessing of the readout data.

A further improvement would be to model the dependency between the geometry of the SPA, the measured resistance in the DC probing, and the resonance frequency of the SPA. This would help to tune the frequency of the SPA more precisely. Up to now, the SPA geometry of a new iteration was changed with respect to the properties of the last SPA iteration. With a more detailed model, it would be possible to estimate the frequency of a SPA already after the DC-probing and not only after it is integrated into the dilution refrigerator. This model could then be integrated into the written drawing routine. Probably the main difficulty in this process would be to characterize the properties of the Josephson Junctions.

Currently, the SPA is used in the non-degenerate, phase-preserving regime. With the same SPA, one could also explore the degenerate, phase-sensitive regime and compare the performance of the two regimes.

Bibliography

1. Clerk, A. A., Devoret, M. H., Girvin, S. M., Marquardt, F. & Schoelkopf, R. J. Introduction to quantum noise, measurement, and amplification. *Rev. Mod. Phys.* **82,** 1155–1208. https://link.aps.org/doi/10.1103/RevModPhys.82.1155 (2 Apr. 2010).
2. Roy, A. & Devoret, M. Introduction to parametric amplification of quantum signals with Josephson circuits. *Comptes Rendus Physique* **17.** Quantum microwaves / Micro-ondes quantiques, 740–755. ISSN: 1631-0705. https://www.sciencedirect.com/science/article/pii/S1631070516300640 (2016).
3. Frattini, N. E., Sivak, V. V., Lingenfelter, A., Shankar, S. & Devoret, M. H. Optimizing the Nonlinearity and Dissipation of a SNAIL Parametric Amplifier for Dynamic Range. *Phys. Rev. Applied* **10,** 054020. https://link.aps.org/doi/10.1103/PhysRevApplied.10.054020 (5 Nov. 2018).
4. Frattini, N. E. *et al.* 3-wave mixing Josephson dipole element. *Applied Physics Letters* **110,** 222603. https://doi.org/10.1063/1.4984142 (2017).
5. Sivak, V. *et al.* Kerr-Free Three-Wave Mixing in Superconducting Quantum Circuits. *Phys. Rev. Applied* **11,** 054060. https://link.aps.org/doi/10.1103/PhysRevApplied.11.054060 (5 May 2019).
6. Sliwa, K. *Improving the Quality of Heisenberg Back-Action of Qubit Measurements made with Parametric Amplifiers* PhD thesis (Yale University, 2016).
7. Schackert, F. D. O. *A Practical Quantum-Limited Parametric Amplifier Based on the Josephson Ring Modulator* PhD thesis (Yale University, 2013).
8. Flurin, E. *The Josephson mixer: a swiss army knife for microwave quantum optics* PhD thesis (Ecole normale supérieure - ENS PARIS, 2014).
9. Caves, C. M. Quantum limits on noise in linear amplifiers. *Phys. Rev. D* **26,** 1817–1839. https://link.aps.org/doi/10.1103/PhysRevD.26.1817 (8 Oct. 1982).
10. Eichler, C., Salathe, Y., Mlynek, J., Schmidt, S. & Wallraff, A. Quantum-Limited Amplification and Entanglement in Coupled Nonlinear Resonators. *Phys. Rev. Lett.* **113,** 110502. https://link.aps.org/doi/10.1103/PhysRevLett.113.110502 (11 Sept. 2014).
11. Dolan, G. J. Offset masks for lift-off photoprocessing. *Applied Physics Letters* **31,** 337–339. eprint: https://doi.org/10.1063/1.89690. https://doi.org/10.1063/1.89690 (1977).